Circular Polarized Super Wideband Antenna with Reconfigurable Filtering Properties

[1]Balu Ashvanth*, [2] D Kanchana, [3]Bactavatchalame Partibane
[1]Dept. of ECE, Vel Tech Rangarajan Dr.Sagunthala R&D Institute of Science and Technology, Chennai-62, India
[2]Dept. of ECE, Sathyabama Institute of Science and Technology, Chennai-119, India
[3]Dept. of ECE, Sri Sivasubramaniya Nadar College of Engineering, Chennai-110, India
drashvanthb@veltech.edu.in, kanchanadurai5@gmail.com, padtibaneb@ssn.edu.in
Mobile: 91-9600096493

Abstract:

There are many uses for this metamaterial antenna such as broad band radars, 5G and automotive applications. With many works of wideband antenna are already available, this work presents a low cost super wide band combined with circular polarization, size compactness and high gain. Super wideband (SWB) is obtained by appropriately etching the patch and inserting a stub into the feed line. To increase the functional bandwidth, that covers 2.69GHz to 22.9GHz frequency range, rectangular slots and the electromagnetic bandgap(EBG) have been included to the ground surface in the interim. A 73% size decrease is achieved using performing partial grinding in addition to step feeding. Unlike traditional approach of employing complex feeding, etching multiple slots across multiple layers, additional elements for realizing circular polarization (CP) with large axial ratio (AR) bandwidth, a simple straightforward approach of using left-handed metamaterial (LHM) underneath the patch introduces circular polarization with wide 3dB axial ratio (AR) bandwidth ranging from 2.78GHz to 21.85GHz. The backing of patch by LHM reverses the radiation in forward direction which greatly enhanced the gain to 5.28dBi which is specific to the designed antenna. The suggested antenna has equipped with reconfigurable filters for tuning to one of three bands of interest whose center frequencies residing at 2.69GHz, 10.5GHz and 18.2GHz respectively across the super wide band that firmly reduces the undesired crosstalk. The vertical slit in the step feed of the suggested antenna enhances impedance matching across a broad operating band.

Keywords: SWB antenna, Left hand Metamaterial, Reconfigurable Filter, Bandwidth

1. Introduction:

These days, there is rapid growth in telecommunication due to the emerging of new technology. Optimizing the performance of the antennae employed at each wireless connection point is crucial to address this. A small, high-gain antenna is needed to minimize the amount of area required. Filtering

characteristics of the antenna are necessary to stop undesired delivery, receiving and disruption. Signal quality is improved and loss is reduced via CP antenna.

A planar antenna that operates in 25 to 33.5 GHz frequency range was presented for internet of things (IoT) application and its axial ratio bandwidth (BW) ranges between 26 to 33.5 GHz was validated in [1]. However, the attained BW was 1.13 to 3.83 GHz and AR BW ranges from 1.18 to 3.82 GHz with the maximum gain of 3dBi. In the vehicular field, a vertical polarized planar dipole antenna is recommended in [2]. Two resonating modes were excited to achieve 3.3 GHz operating bandwidth with a stable radiation pattern having gain variation less than 2.5dB. A patch altered dual ring stacked antenna produces circular polarization across the operating bands in [3]. The gain has been enhanced by interconnecting top radiator with base metallic surface etched with slot. The antenna has only two bands with a 0.1GHz AR bandwidth. The via packed metasurface (MS) is employed to achieve size slimming and wideband, or 5.46 to 8.46 GHz in [4]. When combined with the altered feed, the metamaterial (MTM)-based patch provides compactness. It has more filtering power thanks to the ground slots. Nevertheless, the aforementioned research employed multiple layers, augmenting the antenna's design intricacy and dimensions. The researchers achieved a CP with a stacking structure consisting of twin radiators, involving slots and the edge shortened top radiator in [5]. However, the 0.23GHz BW was incredibly less. An adaptable liquid-crystalline polymer dual-band CP antenna is suggested for the ultra-wideband (UWB) detecting field in the research [6]. To achieve CP with downsizing, it makes use of a slot radiator with quad L-feeders and an ordered phase feeding network. However, the antenna's complexity and manufacturing costs are higher. Cross dipoles, four parasitical radiators, a traveling-wave loop, and several metallic layers were utilized in the work in [7] to achieve CP over its spectrum. The gain of an antenna over the 3–12.4 GHz bandwidth was increased by using a dielectric horn with a insulating lens in [8]. Ground slots and a hook-like feeding probe were used in combination with nonuniform metamaterial cells to generate CP [9]. The low profile of this antenna is $0.06\lambda_O$. A metamaterial polarizer was positioned over a rectangular waveguide's aperture to generate the antenna that has been reported in the literature [10]. The several metamaterial layers that comprise the proposed polarizer have different unit cell sizes. This antenna has a wide impedance band from 7.08 to 13.5 GHz with an AR bandwidth from 9.25 to 12.5 GHz. To improve the X band fan-beam radiation, the antenna proposed was coupled with a metasurface made up of core and impedance matching layers in [11]. The height of an antenna is raised to $0.24\lambda o$ due to the utilization

of numerous layers. A new U-shaped microscopic negative index MTM structure was created and paired with an antenna to increase the gain and bandwidth of an aviation collision avoidance system (ACAS) antenna that uses MTM according to the article [12]. The maximum gain, however, was only 2.09dB when using a single antenna element with a BW of 27.2MHz. The metamaterials presented in [13, 14] use split ring resonators to demonstrate negative refractive index, effective permittivity, and effective permeability, respectively, at dual frequencies (3.32 and 9.24 THz) and over a bandwidth of 0 to 6GHz. A modified annular ring-shaped radiator and a modified step-graded notch packed partial ground plane with a frequency range of 5 GHz to 17.9 GHz was proposed by [15]. In contrast, the generated CP over the operational BW of 4.11–5.24 GHz by using a cross slot in the patch was reported in the work [16]. The suggested antenna operates in the SWB, which spans 2.69GHz to 22.9GHz. This broader bandwidth improves radar performance and allows for better range resolution. The utilization of radar is substantially improved by UWB characteristics of high data rate, minimal power utilization, and affordable cost. The gain of the antenna is increased to 5.28dBi by LHM. Since distant communications depend largely on high-gain antennas, they offer a more accurate means of directing radio signals. The antenna's ground slot and LHM produce circular polarization (LHCP & RHCP), which has the benefits of requiring no polarization correction due to multipath effect. The suggested antenna has equipped with filtering features to tune to required range of frequencies over the super wide band that reduces the undesired crosstalk. Modifications to the Vivaldi antenna include inclined slots, a superstrate, sawtooth-patterned outer edges, an advanced feeding network, crossed tapered slots, and a dielectric lens to achieve ultra-wideband performance, with the highest documented bandwidth of 19GHz, as shown in research [17-22]. The parasitic patches along with complex feeding structures are utilized in [23-25] to realize ultrawide bandwidth with the later having a maximum bandwidth of 8.2GHz. A 3-D printed horn antenna mounted on a cylindrical conductor with ridge for impedance matching at high frequencies and demonstrated to have 16GHz bandwidth is reported in [26]. The application of parallel open stubs and a defected ground structure (DGS) for enhanced high-frequency suppression, with a cutoff frequency around 3GHz, is illustrated in [27]. A comprehensive examination of microwave transmission lines, filters, matching networks, and the basics of antennas was conducted in [28], [29]. Fractal geometry methods were employed to achieve antenna miniaturization as discussed in [30], [31]. A reported miniaturization of up to 70% is noted, along with an increase in bandwidth. Characteristic Mode

Analysis (CMA) is utilized to investigate the modal behavior of circular microstrip patches for achieving pattern diversity in [32].

More information about previous works that was taken into account in the proposed research is provided in section 1. A brief description of the antenna physical details, and development is given in Section 2. Section 3 looks at the LHM structure and related simulation findings. The measurement data will be addressed in section 4, along with the reasoning behind circular polarization in relation to a surface current density.

2. ANTENNA DESIGN AND ANALYSIS

2.1 Antenna Schematic:

A size reduced antenna having broadband property has been depicted in Fig. 1. Parameters of the FR4 substrate used to build the recommended antenna are 40mm of length, 10mm of width, and 0.8mm of thickness. Its dielectric constant is 4.4. In order to attain wideband, a step slot with regular horizontal as well as vertical lengths of C_1 = 2 mm and C_2 = 2 mm splits the resonant patch in half at its center. At ground level directly behind the patch, LHM is added in addition to increasing CP. The CP is realized over most of the working bandwidth by forming a vertical slot at the partial ground with dimensions such as S_G = 17 mm and W_G = 1.5 mm. An inset feeding has been utilized for better matching of impedance, and a rectangle slot is etched to expand the functional bandwidth. Twin rectangle sections with different measurements S_{L1} = 17 mm, S_{L2} = 8 mm, S_{W1} = 1.2 mm, and S_{W2} = 0.8 mm are present in the feedline. Based on the current distribution, the left-handed metamaterial is placed precisely behind the top radiator, which reduces surface current interaction between top and bottom layers. Twin electromagnetic bandgap slots on both sides of ground surface having size of K_1 = 1.5 mm, K_2 = 0.6 mm, K_3 = 0.75 mm, and K_4 = 0.7 mm, improve the bandwidth by 1GHz. To increase the range of impedance bandwidths to 2.7 to 19 GHz, the perpendicular aperture of size C_G = 19 mm and C_{GW} = 1.6 mm is etched in the bottom base plane's center. The longitudinal slot at the ground's center avoids undesired variations toward the inferior portion of the functional BW by adding an extra 1.5GHz of bandwidth. The antenna includes lowpass and highpass filtration based on microstrip lines that run that work together with the feedline to offer bandwidth modification. Digging a metal via near the step slot of the patch allows the axial ratio to be reduced to be below two dB along the operational bandwidth of the antenna. Nearer the inset feed, an inverted "U"-shaped

groove is cut into the patch to give radiation nil at the broad end of the operable bandwidth. The next step is to etch two perpendicular slots along the patch's diagonals to further improve this radiation null. The remaining dimensions are P_1 = 4mm, P_2 = 2 mm. P_L = 13 mm, N_1 = 7mm, N_2 = 1 mm, S_L = 5 mm, L_G = 20.7 mm, G_X = 5 mm, W_G = 1.5 mm, M_L = 14 mm, L_F = 2.35 mm, W_F = 0.8 mm, F_Y = 1.2 mm, W_{F1} = 0.5 mm, F_X = 1.5 mm, L_{F1} = 2.35 mm. The design was started with analytical dimensions, then simulated and optimized.

For a microstrip patch antenna, the wavelength of the signal is determined by its patch size. The design equations of [29] that relate the resonant frequency to the antenna patch dimensions are

$$L = \frac{c}{2f\sqrt{\varepsilon_{eff}}}$$

$$\varepsilon_{eff} = \frac{\varepsilon_r + 1}{2} + \frac{\varepsilon_r - 1}{2}\left[1 + 12\frac{h}{w}\right]^{-1/2}$$

$$W = \frac{c}{2f}\sqrt{\frac{2}{\varepsilon_r + 1}} \qquad (1)$$

Where ε_r is substrate dielectric constant, ε_{eff} is effective dielectric constant, h is the height of the substrate and w is the width of the substrate. The length and width obtained from the aforementioned equation have been rounded to the closest whole numbers of 40mm and 10mm respectively. This results in resonance at a center frequency of 10.4 GHz. After making additional design modifications such as incorporating a partial ground, feed stub, and step feed, the resonance frequency is shifted to 2.72 GHz. Slots and left-handed metamaterials (LHM) are integrated to achieve circular polarization (CP) and enhance gain. Based on transmission line theory [28],[29], a slot located in the upper metallic layer, which is supported by a substrate with a permittivity of 4.4, facilitates the guided wavelength of λ_g

$$\lambda_g = \frac{\lambda_o}{\sqrt{\varepsilon_{eff}}} \qquad (2)$$

Where, λ_g is the guided wavelength and λ_o is the free space wavelength. Initially, a horizontal slot placed at the center of the patch has been adjusted to a width of $\frac{\lambda_g}{4}$. Subsequently, it has been transformed into a meandered slot to create both inductive and capacitive effects within the patch, aiming for size reduction. The impact of this alteration on the resonance frequency is illustrated with a circuit diagram of Fig.2

As the parallel connection of the inductor and capacitor strengthens, the resonance frequency achieved by this radiating patch diminishes [29]. For the proposed antenna, this results in two lower bands being positioned closely together, thereby ensuring a wider bandwidth.

$$f_r = \frac{1}{2\pi\sqrt{L_S C_P}} \tag{3}$$

Where, $L_{S,}C_P$ are the equivalent inductance and capacitance from the above circuit.

The physical characteristics of the different sections in the filters influence their corresponding lumped element values, which subsequently affects their cutoff frequency. The values of the inductors and capacitors presented in the equivalent circuits of low-pass and high-pass filters are derived from their length, or the reverse, as indicated by the equations in Ref [27].

$$L = \frac{Z_O l}{v_c}$$

$$C = \frac{l}{Z_o v_c} \tag{4}$$

Where, l is the length of microstrip line used in filter, Z_O is the characteristic impedance of line section, v_c is the phase velocity. The lumped component values obtained from the equations are L =7.8nH and C =1000pF. These values are fine-tuned by multiplying them by a constant that varies between 0.4 and 0.8 to accommodate different sectional lengths ranging from 1.2mm to 2.35mm, thereby achieving the desired bandwidth. To maximize the circular polarization characteristics of the

proposed antenna, the rectangular patch is made asymmetric by etching rectangular slit at the diagonal corners dimensions of $A_L = 3mm$ and $A_W = 0.3mm$.

As a result of the fringing effect [29], the effective length of the patch is marginally increased than the actual length. Consequently, the substrate length extends beyond the patch and this minor additional length is represented by

$$\frac{\Delta L}{h} = 0.412 \frac{\left(\varepsilon_{reff} + 3\right)\left(\frac{W}{h} + 0.264\right)}{\left(\varepsilon_{reff} - 0.258\right)\left(\frac{W}{h} + 0.8\right)} \quad (5)$$

The radiating patch features etched slots that create inductive and capacitive effects alongside a resistive effect, resulting in a complex effective impedance for the antenna patch. To match this complex impedance with the 50-ohm impedance of the feed, a quarter-wavelength impedance transformer is implemented between the 50-ohm transmission line and the patch. The impedance transformer is strategically positioned at a distance of $S_1 = 3.5$ mm from the patch to ensure that the complex impedance of the patch appears real of 100-ohm to the transmission line. The lower microstrip line of the feed of Fig.3, which serves as a transmission line with a Z_o = 50 ohm impedance, is designed with dimensions of $\boldsymbol{S_{L2}}$ = 8 mm and $\boldsymbol{S_{W2}}$ = 0.8 mm, while the upper microstrip line, which has a $Z_C = 70$ ohm impedance acting as a quarter wavelength impedance transformer, is designed with dimensions of $\boldsymbol{S_{L1}}$ = 17 mm and $\boldsymbol{S_{W1}}$ = 1.2 mm.

The overall length of this microstrip line feed arrangement (Step feed), patch length and the slight additional length due to fringing effects determine the length of the substrate, whereas the substrate width continues to match the patch width. The labels are included for different parts of antenna and a Table 1 that details the benefits of each modifications is included.

2.2 Phases of Antenna Evolution:

The reported antenna is transformed into different versions at various stages has been depicted in Fig. 4, along with the corresponding reflection coefficients. The compact radiating patch fed through a simple rectangle feeding section resonating in 10.4GHz is depicted in stage 1 of Fig. 4. As demonstrated in stage 2, by connecting a stub to the feeding line, double resonance were formed having the respective resonating centers at 2.38GHz and 8.2 GHz. In order to improve impedance matching over the previous iteration, Stage 3 demonstrates the way feeding line has been modified to be composed of two rectangular portions with differing diameters. Divide a radiator by a step slot in stage 4 to get wideband performances from 2.7GHz to 16.3GHz. In stage 5, perpendicular rectangular slots are etched directly beneath the feed line to extend the functional bandwidth to encompass the resonance range between 2.8 to 18GHz. The perpendicular corner slot of the partial ground results in polarization which is circular. Two electromagnetic bandgap ring apertures of base plane are used to further expand the bandwidth; as stage 6 of Fig. 4 shows, this bandwidth extends from 2.7GHz to 21GHz. Fig. 4, Stage 7, illustrates how improving the matching of impedance over an antenna's entire bandwidth can be achieved by adding filters across the feed line. The reduction in size of an antenna [30-31] can be determined by comparing the first order resonant frequency of a basic patch antenna at stage 1 (f_1) with the first order resonant frequency (f_2) of stage 3, which includes a partial ground and step feed, as outlined below.

$$Size\,reduction = \frac{f_2 - f_1}{f_1} \times 100 \tag{6}$$

The resonant frequencies f_1 and f_2 have been found to be 10.4GHz and 2.73GHz, respectively, as shown in Fig. 4. Based on the calculations, the reduction in size has been found to be 73%.

3. Characteristic Mode Analysis:

Characteristic mode analysis (CMA) makes it easier to analyze, synthesize, and optimize antennas by offering knowledge about the physical phenomenon of an antenna of any shape. A collection of orthogonal eigen currents and their corresponding eigenvalues are derived by solving a specialized

eigenvalue equation employing the Method of Moments (MoM) impedance vector. The entire current on the conductor's surface can be expanded into those modes since the eigencurrents are orthogonal. The corresponding mode's radiating behavior can be inferred from the eigenvalues. It is possible to compute the quantities modal significance (MS_n) and characteristic angle (α_n), which are connected to the eigenvalue (λ_n) by [32]

$$MS_n = \frac{1}{|1 + j\lambda_n|}$$

$$\alpha_n = 180^o - \arctan(\lambda_n) \quad (7)$$

For a mode to be a resonant, its modal significance (MS_n)should be equal or nearer to one, eigenvalue (λ_n)must be zero and the corresponding characteristic angle (α_n) should be around 180°. The antenna is designed using computer simulation (CST) tool. CMA of the designed antenna is accomplished by changing the solver setup in CST tool to integral equation solver and setting up the source type in solver parameters to CMA. The additional prerequisites for simulating CMA in CST are as follows. The excitation port must be removed and it is replaced by assigning electric field to Ymin in the boundary conditions while the others directions are kept open. All the conductuing surfaces in the antenna to be modified in to perfect electric condutor (PEC) of neglible thickness with loss free FR4 acting as a substrate. The simulated CMA results are investigated as follows.

Modal Significance (MS) refers to a metric utilized in Characteristic Mode Analysis (CMA) within CST Microwave Studio or similar full-wave electromagnetic solvers, assessing the capacity of a specific mode to radiate at a certain frequency. MS is a real number ranging from 0 to 1, representing the strength or effectiveness of a particular mode in radiating electromagnetic energy.

MS = 1: The mode is in resonance, resulting in maximum radiation.

MS > 0.707: The mode is strongly excited and plays a significant role in radiation.

MS < 0.5: The mode is weakly excited and does not effectively contribute to radiation.

MS = 0: The mode is non-radiating and purely reactive

According to equation (3), for the MS to equal one, the eigenvalue (λ_n) must be zero, and the corresponding characteristic angle (α_n) should be approximately 180 degrees. In the design of antennas, modes are stimulated by making specific structural and design adjustments. During characteristic mode analysis (CMA), CST computes the MS for each mode across a range of frequencies. The MS graphs are typically utilized to identify resonant modes, select feed points, and enhance bandwidth. In this proposed study, the MS graphs have been employed to optimize the operational bandwidth of the antenna being designed. The frequency range that each mode spans can be discerned from the MS graph. As shown in Fig. 5, the initial stage 1 antenna activates three modes, which cover a bandwidth ranging from 4 GHz to 7 GHz. By incorporating zigzag slots in the patch and vertical slots in the ground plane, two additional modes are excited, resulting in an expanded operating bandwidth of 14 GHz. Further etching of longitudinal and electromagnetic bandgap (EBG) slots in the partial ground extends the bandwidth from 2.69GHz to 22.9 GHz. Three resonant modes are induced by a straightforward rectangular patch in Fig. 5(a) with a partial ground plane and step feed. While mode 3 predominates between 5GHz and 7GHz, modes 1 and 2 cover the frequency range between 4GHz and 7GHz. Two further modes, 4 and 5, with maximum MS between 10GHz and 15GHz, are produced by adding a stub to the feed line and etching vertical and corner slits in the partial ground, as seen in Fig. 5(b). The antenna's operational frequency range is expanded from 3GHz to 15GHz as a result of these changes, which cause initial modes 1 and 2 to achieve their maximum from 3GHz itself. Mode 6, which operates up to 19GHz, is introduced by the etching of two EBG slots and a longitudinal slot in the ground plane. As shown in Fig. 5(c), modes 7 and 8 were created by the incursion of rectangle slots at the diagonal sides of the patch and filtering structure. These modes covered up to 25GHz from 10GHz. The antenna can be referred to as a super wide band antenna because the combination of all eight modes increases the operational frequency range. The characteristic angle and eigenvalue of the mode must be closer to 180 degrees and zero, respectively, for it to be resonant. According to Fig. 6 examination of the characteristic angle and eigenvalue, the lower order modes (modes 1 and 2) are more prevalent at lower frequency ranges, while the higher order modes (modes 6, 7, and 8) are more prevalent from mid to higher frequencies.

Since the resonated triple modes are common between 3GHz and 7GHz, the electric field is simulated at 6.5GHz for stage 1 of the antenna construction. As seen in Fig 7(a), the Mode 1 field strength is highest at the patch's edges and oscillates back and forth along those edges on a regular basis. In contrast, as Fig 7 (b) illustrates, the field strength for Mode 2 peaks over the feedline, and its direction varies regularly along the feedline. Mode 3's current distribution is nearly identical to Mode 1's, however the direction of the current oscillation is slightly different. Right hand circular polarization (RHCP) is the result of the fields in this mode revolving counterclockwise with respect to time.

As shown in Fig.8, the electric field distribution is retrieved at 12GHz from the antenna's stage 2's five resonant modes, which span the frequency range of 5GHz to 15GHz. In mode 1, the electric field is evenly dispersed throughout the slits, patch edge, and feed line. The field only appears in the Mode 2 feed, oscillates frequently over the feed length, and is at its strongest when compared to previously. With the exception of the direction of vibration, the mode 3 field distribution combines the characteristics of modes 1 and 2, as mode 3 fields are more bidirectional along the feed edge. The etching of longitudinal slots in the ground and zig zag slits in the patch introduces mode 4 and 5. Thus electric field is concentrated across the patch and longitudinal slot of ground for Mode 4 and Mode 5 of above Fig.8. The difference among them is the field intensity, as field of mode 4 is more ground oriented while mode 5 fields are reaching their peak at the patch slits.

The inclusion of LHM behind the patch and their interaction through metallic via provides Mode 6 and thus fields are tended to be maximum at the LHM as depicted by Fig. 9 (a). The fields are rotating clockwise at every time instant and thus renders LHCP at higher order modes. The EBG structure etched at the ground introduces Mode 7 and hence field distribution is more across the EBG as illustrated by Fig. 9 (b). The field intensity varies periodically from left to right EBG and they are directed in and out of the EBG. The addition of filtering structures around the feed line not only improves the impedance matching but also gives rise to mode 8 whose fields are maximized in the filters as shown in Fig. 9 (c). These fields are interacting with the feed line periodically.

4. Equivalent Circuit of Antenna

Fig. 10 (a) shows the equivalent circuit [32] along with radiation resistance of the suggested antenna. The equivalent circuit was designed using the Advanced Design System (ADS) software, and the values of its passive components were optimized to improve the approximation of the simulation results. Fig. 10 (a) displays the comparable equivalent network of the proposed LHM. LHM characteristics are produced by the middle inductor when the capacitor and inductor are arranged in parallel. The patch with meandered slot is indicated with parallel combination of RLC and metallic via by inductance. The bottom partial ground plane has EBG and longitudinal slots which are indicated by LC and RLC combinations of specific values respectively. There is high bandwidth agreement between the CST antenna configuration and its ADS equivalent circuit counterpart, according to a comparison of their reflection coefficients as shown by Fig. 10 (b).

Having designed the antenna using the full wave electromagnetic simulator CST, the reflection coefficient S11 is extracted over the frequency of interest. Based on the antenna design, a circuit using passive components such as resistors, inductors, and capacitors (RLC) is created in the ADS circuit simulator. The values of the RLC components are adjusted continuously to match the S11 of the electrical circuit with that of the CST model. This method converts the antenna's electromagnetic behaviour into an electrical representation. This is particularly advantageous for analysis, simulation, or integrating antennas with other circuit elements (for example, in RF front ends or sensors). The equivalent circuit of the proposed antenna is elaborated in the Table.2

To create the equivalent circuit of an antenna in ADS, it is necessary to acquire input impedance (S_{11}) data for the antenna, which can be sourced through CST simulation. Based on the impedance characteristics, a suitable circuit configuration with several RLC branches has been selected for this broadband design. In the schematic window of ADS, lumped components (R, L, C) are extracted from the component library and organized according to the chosen configuration, linking the circuit to a 50-Ω port (Term) to imitate the feed. An S_Param controller is added to define the frequency range for the simulation, and variables are designated for each component to facilitate tuning. By executing the simulation, the resulting S-parameters or input impedance are contrasted with the reference data from the antenna. The ADS optimization tool is employed by configuring Opt_Param for the circuit components and establishing Opt_Goal functions (such as attaining a specific S_{11} magnitude or matching impedance throughout the desired bandwidth). Through a cycle of iterative tuning and optimization, the equivalent circuit accurately represents the S_{11} characteristics of the antenna.

5. Left Handed Metamaterial (LHM):

The properties of an electromagnetic element are its electric permittivity (ε) and magnetic permeability (μ). Right-handed (RH) materials have both ε>0 and μ>0, indicating a positive (β>0) phase constant for wave propagation. Positive or Right-handed Metamaterial(RHM) is a is the term used to describe this kind of material and it readily available in nature. The negative, LHM, has μ>0 and ε<0 and it has to be produced. The manmade materials called LHMs are made to have specific properties which aren't found in naturally available things. Because of the unique properties of these materials, it is possible to create powerful electromagnetic filters, antennas, which are not achievable with traditional methods. When an electromagnetic wave strikes a material with a negative refractive index (LHM), it bends in the opposite direction because the angle of refraction is larger than the angle of incidence. If an antenna's radiating patch is backed by LHM, this phenomenon reverses the waves, increasing the gain and front-to-back ratio in a forward direction. Periodic current circulation is established in the LHM by drilling and positioning a metallic via between the slotted patch and the LHM, which causes current to flow from the patch to the LHM. This periodicity causes the current

direction to change clockwise at each specified time instant, giving the intended antenna circular polarization.

Fig. 11 shows the design layout of left handed metamaterial. Metamaterial is made up of FR4 dielectric material as substrate of thickness 0.8mm. The middle inductor in a parallel arrangement of capacitor and inductor generates LHM characteristics. At 3.2GHz, the modelled left-handed metamaterial produces permittivity in the negative; as a result, the corresponding response agrees with the left-hand material characteristics. The parametric curve in Fig 12 illustrates the LHM features of this unit cell, which include negative permittivity and negative permeability in addition to a negative refractive index(RI). The simulation and design processes were conducted using the CST microwave studio tool. Analyzing and justifying the LH function of the suggested design is possible by utilizing the S-parameters to calculate the permittivity (ε), permeability (μ), and refractive index (n). The physical dimensions are $\boldsymbol{H}$=13mm, $\boldsymbol{W}$=11mm, $\boldsymbol{G_Y}$=0.4mm, $\boldsymbol{G_X}$=1.1mm, $\boldsymbol{U}$=4mm, $\boldsymbol{Q}$=5mm, and $\boldsymbol{R}$=8mm. Loading antennae with LHM structure allows radiation to be manipulated inside the antenna system. Antenna downsizing is achieved along with geometries' low resonance. Additionally, modifying electromagnetic waves makes it possible to achieve CP enhances gain and bandwidth. Behind the radiating patch, which is a component of the ground plane, is where the LHM is located. With more discontinuities provided by this ground plane adjustment, the antenna design radiates greater power and absorbs less energy, yielding a maximum gain of 5.28dBi.

As illustrated in Fig. 13, it is crucial to analyze the surface current distribution at different time intervals to demonstrate the circular polarization (CP) mechanism of the proposed antenna. The rectangular monopole antenna generates linear polarization (LP). A broad impedance bandwidth is achieved when the fundamental mode is divided into two separate degenerate modes due to the step slot located in the center of the patch. The phase differences between these degenerate modes, created by the corner rectangular slot in the ground, influence the current's direction, causing it to shift left or right at phases of 90° and 180°. The introduction of the left-handed material (LHM) produces the

necessary current disruptions that enable the current to move upward and downward at 0° and 270°, which is essential for right-hand circular polarization (RHCP). The inset feed's depth impacts the phase difference between the current vectors; an increased depth results in a larger phase difference. Consequently, the inset feed is designed to accurately produce RHCP.

6. Discussion of results:

Fig. 14 shows the axial ratio graph illustrating the CP behavior of reported design. The designed antenna exhibits good circular polarization capabilities and has an simulated AR value of under 3dB between 2.78GHz to 21.85GHz. 3.27GHz to 21.8GHz is the measured 3 dB AR bandwidth. The fabrication deviation causes the measured AR to degrade to 2–3 dB. The impedance bandwidth is slightly ahead of the AR bandwidth. The AR graph clearly exhibits the presence of CP on the proposed antenna.

The microstrip reconfigurable filter integrated with the feeding line consists of a low pass filter (LPF) and a high pass filter (HPF) that dynamically adjusts the antenna to the preferred frequency band. Based on their frequency response features, these LPF and HPF allow the passage of low and high frequencies when combined with the antenna. By cascading the LPF and HPF, a band pass filter (BPF) is created, which enables the transmission of mid frequencies within the antenna's spectrum. Consequently, this reconfigurable filter provides access to various bands or services within the antenna's designated frequency range, minimizing unnecessary disruption or interference across the extensive operating range of 2.69GHz to 22.98GHz. As shown in Fig. 15, a pin-diode and the associated active and passive elements for biasing are assembled on a board. The direct current (DC) source drives the diodes, that are activated and coupled in the appropriate locations of P1, P2, and P3 within the built antenna. The VNA was also utilized for measuring the other reflection properties.

As illustrated in Fig. 16(a), the high-pass and low-pass filters are strategically placed around the feeding structure. The high-pass filter features a “T” shaped component. A narrow gap (0.3 mm) at the center of the T-resonating element facilitates high-pass filtering, as depicted in Fig 16(b), along with its equivalent circuit. The circuit has capacitors C_1 and C_2 at the middle which accepts input signal and passes high frequencies to feed line through resistor R_1 while inductor bypasses low

frequencies to ground. The filtering process is described in the context of pin diodes. The P_2 and P_3 pair of switches that are currently being used. P_3 is positioned at the center of the aperture, while P_2 links the feeding line to the "T" resonator. As illustrated in Fig.16(d), the reconfiguration filter functions as a high-pass filter when both P_2 and P_3 are activated to connect the feed to HPF, and diode P_1 is kept off to isolate the LPF. This configuration enables the radiator to operate within the 14GHz to 23GHz resonance range. The low-pass filter consists of two closely spaced twin L-shaped resonating elements that are linked to a feeding line through a pin-diode (P_1), with the corresponding equivalent circuit confirming its low-pass behaviour shown in Fig. 16(c). When P_1 is triggered, it connects the LPF to the antenna feedline, allowing the antenna to operate at a frequency of 2.69GHz in the low-pass mode as shown in 16(e). Due to the arrangement of these filters, the reconfiguration filter serves as a band-pass filter when P_2, P_2 and P_3 are all activated, cascading the LPF and BPF together. As demonstrated in Fig. 16(f), the antenna's operational bandwidth is narrowed to 10.5GHz, which is close to the center frequency, in band-pass mode.

The BAR64 pin diode is utilized for the reconfiguration of the antenna's bandwidth. The equivalent circuit, along with the values of lumped elements, is illustrated in Fig.17. In the ON state, the pin diode functions as a current-controlled resistor in series with a slight package inductance. Conversely, in the OFF state, it acts as a small capacitor in series with the same inductance.

A constructed model of the recommended SWB antenna is depicted in Fig. 18. The antenna has three working types: lowpass, highpass, and bandpass. Circular polarization can be achieved more easily and gain can be increased by adding LHM below the monopole radiator. The antenna dimension is reduced to $0.4\lambda_o$ x $0.1\lambda_o$, with respect to the lower resonance. A VNA is used to measure the S11 of the generated antenna, and the comparison been made with the simulation's outcome. The S11 clearly reveals that the reflected signal power reflected to the incident signal power on the interconnect of two ports. Here the ports are associated with antenna and transmission line/ coaxial cable. The reason for the discrepancies may be due to connector loss, dielectric loss, uneven copper coating on the FR4 substrate, near field scattering objects, faults in soldering and fabrication. The 20.3GHz of bandwidth is one of the most crucial considerations for the suggested antenna. The resonant frequencies f_1 and f_2 have been found to be 10.4GHz and 2.73GHz, respectively. Based on

the calculations, the reduction in size has been found to be 73%. With this produced antenna on the side that receives signals and the horn functioning as the transmit antenna, the distributions of radiation in the anechoic chamber have been measured.

Fig. 19 and 20 shows the radiation patterns in the zoy (E-plane) and xoy (H-plane) planes respectively. The simulated radiation characteristics at 3GHz, 11GHz and 16GHz were nearly identical to their observed versions over this wide operating bandwidth. The radiation pattern at 3GHz is dumbbell shaped while those at 11GHz and 16GHz were almost covering four quadrants. The designed antenna is effective enough for specific polarization as it has low cross polarization levels as illustrated in radiation pattern plots. Several factors can lead to the contrast among the results of simulation and experiment, including the following: idealized theoretical representations of the CST simulation's antenna configurations, small variations in the properties and dimensions of the material, fabrication and soldering errors, shifts in stray fields, and some inaccurate measurements.

For a SWB antenna covering the huge bandwidth, it is essential to fix the antenna's size fixed; smaller is preferable. To verify these requirements, profile compression has been made that decreases the design dimension or size. The antenna's area is regarded as its size. Therefore, a combination of width and length (W×L) is used to determine size. It is possible to determine the antenna's guiding wavelength [29] by

$$\lambda o = \frac{c}{f\sqrt{\varepsilon_r}} \qquad \ldots(8)$$

where, c = speed of light (3×10^8 m/s), f=center frequency of operational bandwidth. The bandwidth ratio [29] is frequently utilized for estimating bandwidth, which is expressed as

$$BW = \frac{f_h}{f_l}:1 \qquad \ldots(9)$$

For the developed antenna, the bandwidth measures 8.54:1, which has been compared with similar works in the comparison Table 3. The comparative assessment of various antenna designs from

references [1], [2], [3], [4], [5], [6], [9], [16], and [19] highlights the advantages of our proposed antenna. In terms of compactness, our design occupies merely $0.04\lambda_o^2$, which represents the smallest footprint, only matching [3] ($0.04\lambda_o^2$) and being significantly smaller than [1-3, 5, 6, 9, 16, 19]. When it comes to impedance bandwidth, our antenna achieves an impressive ratio of 8.54:1, which outperforms all the specified references. A major strength of our work is its axial ratio bandwidth of 19 GHz, considerably higher than that of [1], [4], [5], [6], and [16], while references [2], [3], [9], and [19] do not provide support for circular polarization. In terms of gain, our antenna delivers 5.28 dB, which, although lower than [5] and [9], remains competitive and exceeds the performance of [1], [2], and [4], closely matching [6] and [16]. Moreover, in contrast to [1], [2], [4], [6], [9], [16], and [19], our design includes physical filters, akin to [3] and [5], which contribute to improved bandwidth and polarization performance. Apart from reference [4], there are no other studies that provide polarization reconfiguration or any other type of reconfiguration. The research in [19] achieved a peak efficiency of 90%, whereas the current proposal attains a next highest efficiency of 85%. In summary, when compared to all the aforementioned references, our antenna is distinguished by its compact size, ultra-wide impedance bandwidth, and outstanding axial ratio bandwidth, while still achieving a satisfactory gain level and efficiency.

Fig. 21 shows the fluctuation of the gain over the functional bandwidth and the comparison has been made between simulated and measured gain. There is slight deviation among the measurement and simulation results across the mid frequencies. The antenna gain is increased at its lower frequency of operation by using LHM. It reaches its peak at 19GHz and then starts to decrease. This work focuses on services that encompass automotive, 5G, and radar technologies, with frequencies ranging from 2 to 27 GHz. The use of low-cost FR4 substrate results in very minimal gain at lower frequency bands, which is crucial for most of the mentioned applications. Therefore, incorporating a left-handed metamaterial (LHM) behind the radiating patch is employed to redirect electromagnetic waves in the forward direction at lower frequencies, enhancing the gain to the required levels for the application. The antenna designed without the LHM achieves a gain between -0.93dBi and 0.5dBi for frequencies from 2.69 GHz to 8.5 GHz. In contrast, integrating the LHM raises the gain to a range of 0.9dBi to 3.4dBi throughout the same frequency interval of 2.69 GHz to 8.5 GHz. Consequently, a maximum gain improvement of 2.9 dBi has been observed. Thus, the significant increase in gain within this

lower frequency range is deemed suitable for estimating the operational bandwidth, as it encompasses essential services along with enhanced impedance matching.

The automotive sector that facilitates vehicle-to-vehicle (V2V) and vehicle-to-infrastructure (V2I) communications operates within the 5.850 – 5.925 GHz range, while vehicle-to-everything (V2X) specifically utilizes the 5.9 GHz band. In contrast, 5G technology functions within a frequency range of 3.3–3.670 GHz. Radar systems, which differ based on their applications, are utilized in areas like weather monitoring, aviation, and military operations. A broad array of frequency bands, including S(2-4GHz), C(4-8GHz), X (8-12GHz), and K(18-17GHz), has been employed for the radar applications mentioned above.

7. Conclusion:

A small UWB antenna operating in the 2.69GHz to 22.98GHz frequency band has been presented. The antenna that has a LHM unit cell built in it can achieve CP and gain improvements of up to 5.28dBi. The CMA analysis was done to get greater insight in to the mode generation and its influence in the bandwidth expansion. For the recommended left-hand metamaterial, refractive index, permittivity, and permeability were simulated as it plays a vital role in improving antenna performance. Three separate pass bands can be provided over the operational bandwidth by the reconfiguration filter. To verify the modeling results, a working model of the suggested circular polarization SWB antenna is built and verified. The proposed antenna can be utilized in the automotive industry, 5G systems, and radar systems that covers a wide frequency range.

Funding Statement: No fund is obtained from any financing organization.

Conflict of Interest: There is no conflict of interest

Data Availability: Data are available with the authors. On request, it will be given

Ethics statement: This work is original. It is submitted only to this journal and not in elsewhere

References:

[1]. Qin Zhou, Xue Ren. “An ultrawideband circularly polarized antenna with traveling-wave loop”, *IEEE Ant. Wireless Propag. Lett.*, 23(8), pp.2331 – 2335 (2024). **DOI:** 10.1109/LAWP.2024.3389058

[2]. Sun Shuai, Jun-Hui Ou , Huafeng Su, et. al. "Ultra-wideband omnidirectional antenna with stable radiation patterns using CMA", IEEE Trans. Veh. Tech., 73(7), pp.10788-10792 (2024). **DOI:** 10.1109/TVT.2024.3368222

[3]. Balu Ashvanth. "A compact high gain filtering patch antenna for multiband wireless system", Eng. Res. Express., 5(045067), pp.1-10 (2023). **DOI** 10.1088/2631-8695/ad0996

[4]. Youngje Sung. "Simple slot antenna with polarization diversity", *IEEE. Ant. Wireless Propag. Lett.*, 21(4), pp.690–694 (2022). **DOI:** 10.1109/LAWP.2022.3141797

[5]. Guangshang Cheng , Jian Zhou, Lixia Yang, et al. "A stacked circularly polarized filtering antenna with crossed slot", *IEEE Ant. Wireless Propag. Lett.*, 22(12), pp.2935–2939 (2023). **DOI:** 10.1109/LAWP.2023.3305600

[6]. Yongjian Zhang, Yue Li, Mingzhe Hu, et al. "Dual-band circular-polarized microstrip antenna for ultrawideband positioning in smartphones with flexible liquid crystal polymer process", *IEEE Ant. Wireless Propag. Lett.*, 71(4), pp.3155 –3163 (2023). **DOI:** 10.1109/TAP.2023.3247130

[7]. Ubaid Ullah, Slawomir Koziel, Anna Pietrenko, et al. "Highly integrable planar-structured printed circularly polarized antenna for emerging wideband internet of things applications in the millimeter-wave band", Scientific Reports, 14(10138), pp.1-11 (2024). **DOI**: https://doi.org/10.1038/s41598-024-60678-3

[8]. Renato Cicchetti, Valentina Cicchetti, Antonio Faraone, et al. "A wideband high-gain dielectric horn-lens antenna for wireless communications and UWB applications", *IEEE Ant. Wireless Propag. Lett.*, 71(2), pp.1304 –1318(2023). **DOI:** 10.1109/TAP.2022.3228384

[9]. Kang Yu Yang, Wen Jian Zhu, Liang Hua Ye, et al. "Metamaterial-based low-profile broadband in-band full-duplex antenna", *IEEE Ant. Wireless Propag. Lett.*, 22(8), pp.1942 – 1946 (2023). **DOI:** 10.1109/LAWP.2023.3270167

[10]. Quan-Wei Lin, Shaker Alkaraki, Hang Wong, et al. "A wideband circularly polarized antenna based on anisotropic metamaterial", *IEEE Trans. Ant. Propag.*, 71(2), pp.1254 – 1262 (2023). **DOI:** 10.1109/TAP.2022.3225157

[11]. Xue Ren, Youpeng Bao, Zehai Wu, et al. "A low-profile wideband metasurface antenna with fan-beam radiation", IEEE Open Jourl. of Ant. Propag., 3(2), pp.745 - 751 (2022). **DOI:** 10.1109/OJAP.2022.3187378

[12]. M. Pallavi, Pramod Kumar, Tanweer Ali, et al. "Design and experimental study of a coupled u and l-shape negative index metamaterial for aircraft navigation applications", *IEEE Access*, 12(1), pp.16127 - 16150 (2024). **DOI:** 10.1109/ACCESS.2024.3358898

[13]. Anowarul Haque, M.T. Islam, Ismail Hossain, et al. "Left-handed metamaterial based on circular split ring (CSRR) resonator for microwave sensing Application", *Optical Materials*, 152,(2), pp.1-8 (2024). **DOI**: https://doi.org/10.1016/j.optmat.2024.115480

[14]. Tayaallen Ramachandran, Mohammad Rashed Iqbal Faruque and K. S. Al-mugren. "Symmetric left-handed split ring resonator metamaterial design for terahertz frequency applications", *Scientific Reports*, 13(21828), pp.1-12 (2023). **DOI**: https://doi.org/10.1038/s41598-023-49202-1

[15]. Tarik El-Arrouch, Sudipta Das, Tanvir Islam, et al. "Slots and stubs incorporated annular ring-shaped compact microstrip antenna with circular polarization characteristics for wireless UWB communication systems", *Phys. Scr.*, 99(065519), pp.1-10 (2024). **DOI**:10.1088/1402-4896/ad451d

[16]. Meenakshi Tripathi, Anand Sharma and Vinay Kumar. "Metasurface loaded dual port circularly polarized dielectric resonator antenna with reduced RADAR cross section and mutual coupling features", *Phys. Scr.*, 1(085501), pp.1-8, 99 (2024), **DOI**: 10.1088/1402-4896/ad5a54

[17]. Ababil Hossain, Stephen Pancrazio, Tyler Kelley, et al. "A compact and low-profile high-gain multilayer vivaldi antenna based on gradient metasurface superstrates", *IEEE Ant. Wireless Propag. Lett.*, 24(6), *pp*.1537-1541 (2025). **DOI:** 10.1109/LAWP.2025.3542315

[18]. Hao Zhang and Fang Zhang. "A novel ultrawideband miniature vivaldi antenna with sawtooth outer edges and inclined elliptical slots", *IEEE Ant. Wireless Propag. Lett.*, 23(9), *pp*.2708-2713 (2024). **DOI:** 10.1109/LAWP.2024.3405007

[19]. Xiao-Yuan Sun, Bian Wu, Hong-Hao Zhang, et al. "Ultrawideband circularly polarized halved-type vivaldi antenna with symmetrical radiation pattern" *IEEE Ant. Wireless Propag. Lett.*, 23(2), *pp*.633-637 (2024). **DOI:** 10.1109/LAWP.2023.3331383

[20]. Xiaoyu Liu , Yongzhong Zhu and Wenxuan Xie. "Miniaturized ultrawideband circularly polarized antenna with folded arms inspired by the conventional vivaldi antenna", *IEEE Ant. Wireless Propag. Lett.*, 22(12), *pp*.2768-2772 (2023). **DOI:** 10.1109/LAWP.2023.3275322

[21]. Yang Cheng , and Yuandan Dong, "Ultrawideband shared-aperture crossed tapered slot antenna for 5G applications", *IEEE Ant. Wireless Propag. Lett.*, 22(3), *pp*.472-476 (2023). **DOI:** 10.1109/LAWP.2022.3215644

[22]. Weijun Huang, Yu Xiao, Guoqiang Zhao, et al. "Ultrawideband tapered slot antenna with phase-correcting dielectric lens loaded", *IEEE Ant. Wireless Propag. Lett.*, 23(12), *pp*.4218-4222 (2024). **DOI:** 10.1109/LAWP.2024.3440052

[23]. Dawei Ding, Junfeng Chen, Guangwei Fan, et al. "Ultrawideband horizontally polarized omnidirectional antenna by using multiple feeds", *IEEE Ant. Wireless Propag. Lett.*, 24(1), *pp.*108-112 (2025). **DOI:** 10.1109/LAWP.2024.3389058

[24]. Tian Lou , Zhongxiang Shen and Xue-Xia Yang. "Circularly polarized UWB antenna based on a single-folded substrate", *IEEE Ant. Wireless Propag. Lett.*, 23(7), *pp.*2195-2200 (2024). **DOI:** 10.1109/LAWP.2024.3384979

[25]. Sen Yan, Xiaohan Zhai, Hongwei Ren, et al. "A low-profile dual-polarized omnidirectional antenna for WLAN/UWB applications", *IEEE Ant. Wireless Propag. Lett.*, 23(5), *pp.*1433-1437 (2024). **DOI:** 10.1109/LAWP.2024.3358324

[26]. Yifan Wang, Teng Li, and Wenbin Dou. "Ultrawideband 3-D printed endfire tem horn antenna mounted on a cylinder conductor", *IEEE Ant. Wireless Propag. Lett.*, 22(8), *pp.*2022-2026 (2023). **DOI:** 10.1109/LAWP.2023.3271849

[27]. Jongkuk Park, Jeong-Phill Kim, and Sangwook Nam. "Design of a novel harmonic-suppressed microstrip low-pass filter", *IEEE Microwave & Wireless Comp. Letts.*,17(6), pp.424-426 (2007). **DOI:** 10.1109/LMWC.2007.897789

[28]. Pozar. D. M. "*Microwave engineering"*, International adaptation, 4th Edn, pp.1-752, Wiley, University of Massachusetts at Amherst (2012).

[29]. Balanis. C. A. "*Antenna theory: analysis and design"*, Design and analysis, 4th Edn, 1-1073, Wiley, Arizona State University, USA (2016).

[30]. Eduardo .A, Souza .M, Phelipe .S. "Miniaturization of a microstrip patch antenna with a koch fractal contour using a social spider algorithm to optimize shorting post position and inset feeding", *Int. Jour. Ant. & Propag., 4(6284830), 1-10 (2019).* **DOI:** https://doi.org/10.1155/2019/6284830

[31]. Partha Kumar Deb and Tamasi Moyra. *"*Miniaturization of microstrip patch antenna using fractal antenna design", *Proceedings of International Conference on Computational Intelligence & IoT (ICCIIoT), Malta, pp.1-7 (2018).* **DOI:** https://doi.org/10.35444/IJANA.2024.16301

[32]. Changjiang Deng, Zhewei Zhao, Weihua Yu. "Characteristic mode analysis of circular microstrip patch antenna and its application to pattern diversity design", IEEE Access, 10(1), pp.2399-2407 (2022). **DOI:** 10.1109/ACCESS.2021.3139316

Fig. 1: Antenna schematic (a) Top, (b) Bottom (c) E.B.G

Fig.2 LC network

Fig. 3 Quarter wavelength impedance matching

Fig. 4: Transformation steps of designed antenna (a) Stage1-2, (b) Stage 2-3, (c) Stage 3-4, (d) Stage 4-5, (e) Stage 5-6, (f) Stage 6-7

Fig. 5: Modal Signifance of different stages of proposed antenna (a) Stage1, (b) Stage2, (c) Stage3

Fig. 6: Simulated results of (a) Charactersitic angle, (b) Eigenvalue

Fig 7: Field distribution of (a) Mode 1, (b) Mode 2, (c) Mode 3

Fig. 8: Field distribution of (a) Mode 1, (b) Mode 2, (c) Mode 3, (d) Mode 4, (e) Mode 5

Fig. 9: Field distribution of (a) Mode 6, (b) Mode 7, (c) Mode 8

Fig. 10: Antenna (a) Equivalent circuit, (b) Circuit & schematic S11 comparison

Fig. 11: LHM unit cell

Fig. 12: Left hand metamaterial: (a) Permeability, (b) Permittivity, (c) Refractive index

Fig. 13: Surface current direction for different phases of (a) 0^{o}, (b) 90^{o}, (c) 180^{o}, (d) 270^{o}

Fig. 14: AR graph

Fig. 15: Simulation and measurement of S11

Fig.16: Reconfigurable filters (a) Reconfiguration filter (b) High pass filter, (c) Low pass filter (d) High-pass response, (e) Low-pass response, (f) Band-pass response

Fig. 17: Equivalent circuit of pin diode in (a) ON state, (b) OFF state

Fig. 18: The antenna (a) Fabricated layout with measuring arrangement, (b) S11 comparison

Fig. 19: E plane Radiation patterns at (a) 3GHz, (b) 11GHz, (c) 16GHz

Fig. 20: H plane Radiation patterns at (a) 3GHz, (b) 11GHz, (c) 16GHz

Fig. 21: Gain vs Frequency plot

Table 1: Modifications and their improvements

Table 2 Details of equivalent circuit

Table 3: Comparing of this research to the related article

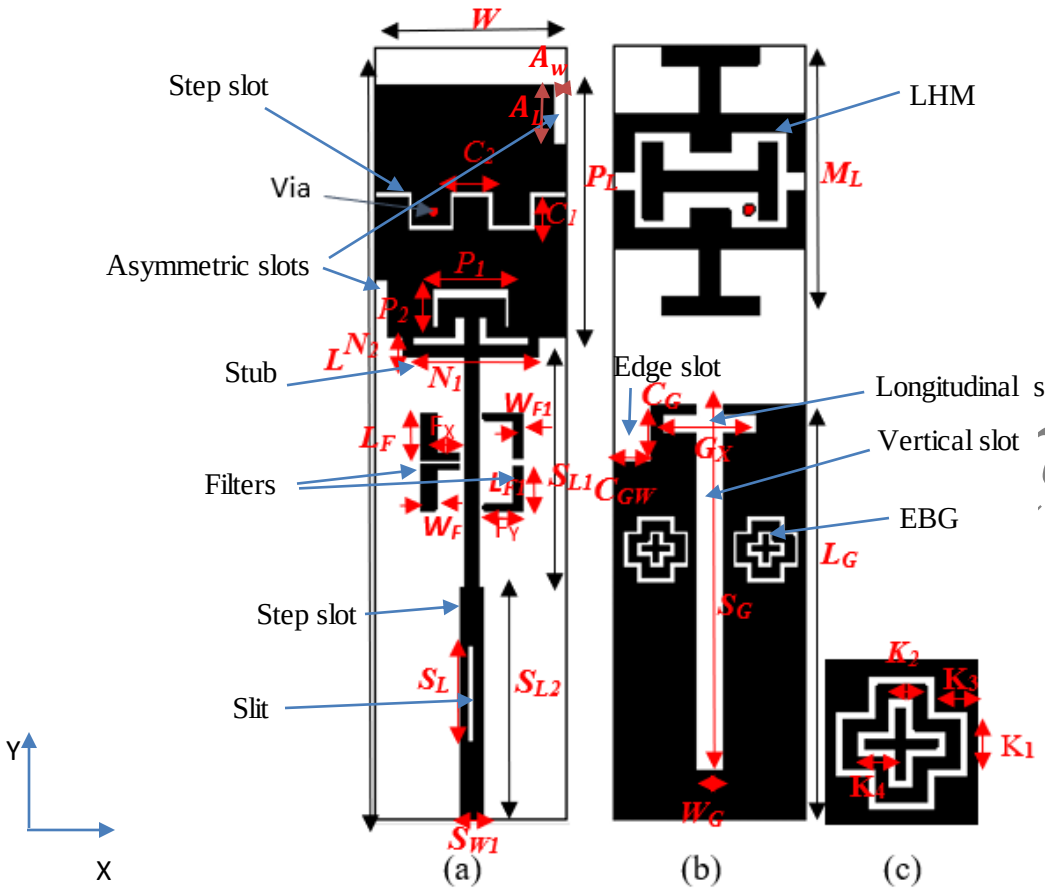

Fig. 1 Antenna schematic (a) Top, (b) Bottom (c) E.B.G

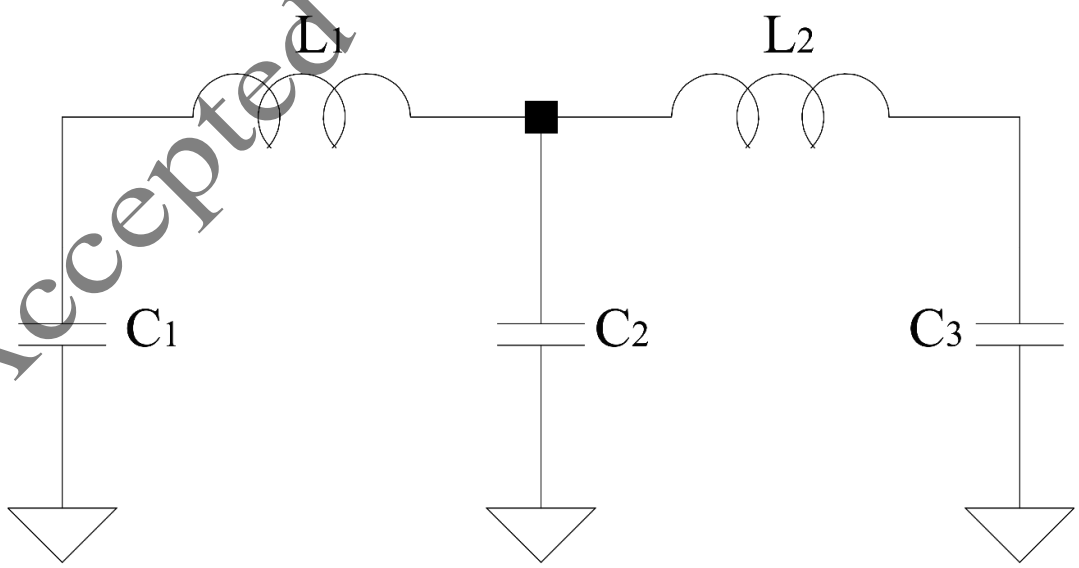

Fig.2 LC network

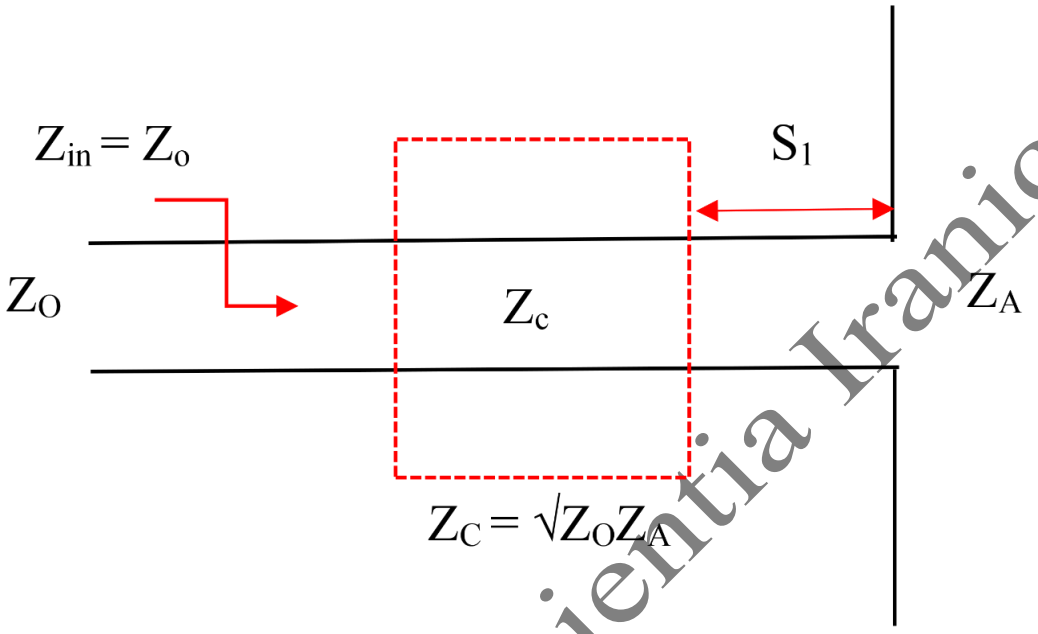

Fig. 3 Quarter wavelength impedance matching

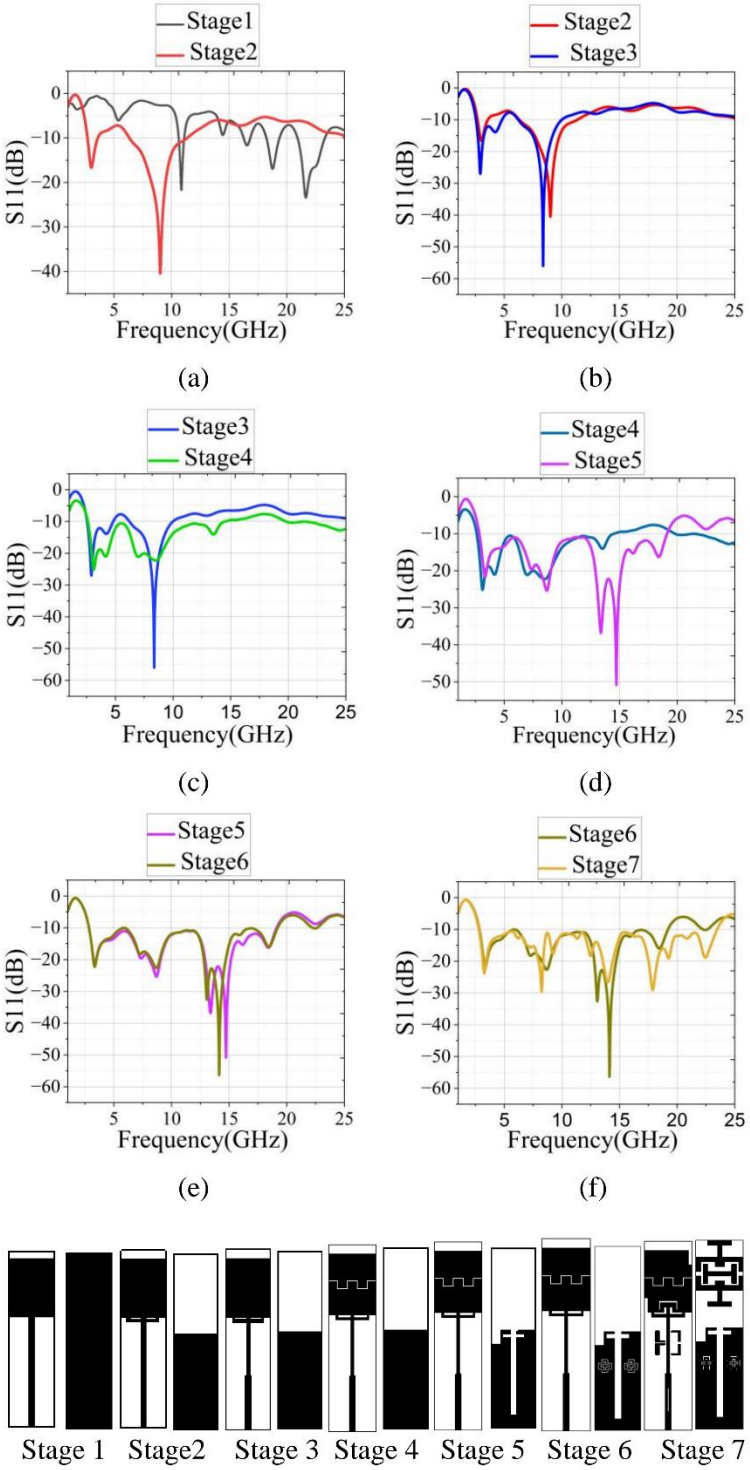

Fig. 4: Transformation steps of designed antenna (a) Stage1-2, (b) Stage 2-3, (c) Stage 3-4, (d) Stage 4-5, (e) Stage 5-6, (f) Stage 6-7

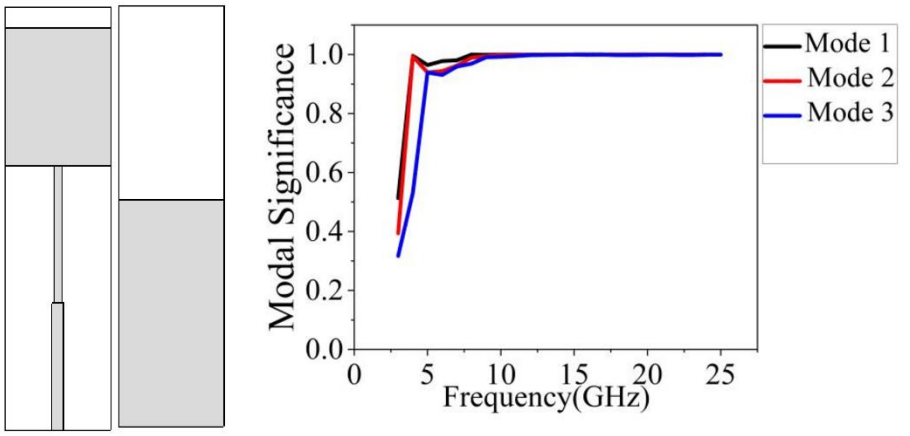

(a)

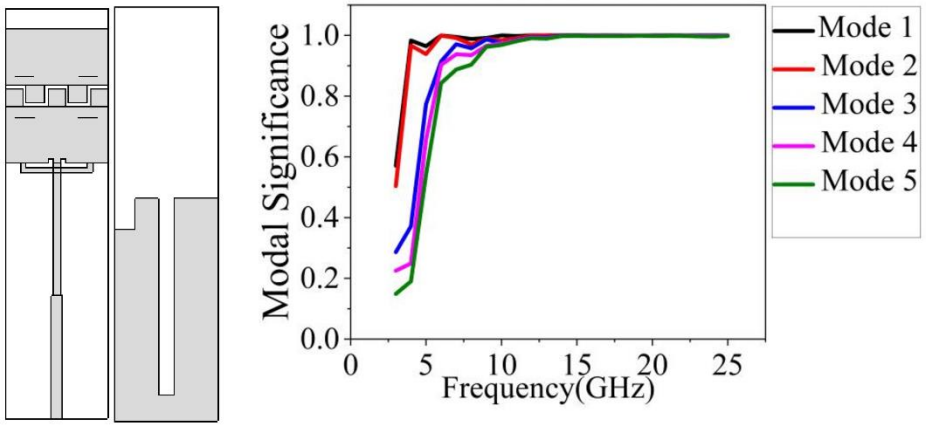

(b)

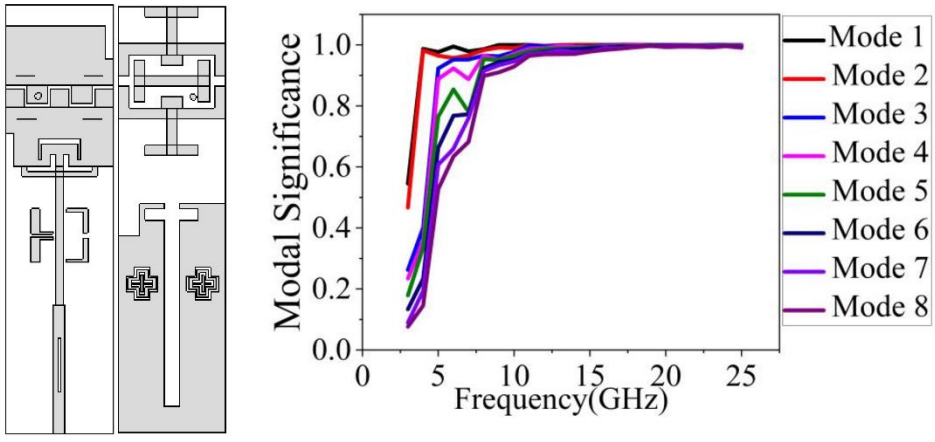

(c)

Fig. 5: Modal Signifance of different stages of proposed antenna (a) Stage1, (b) Stage2, (c) Stage3

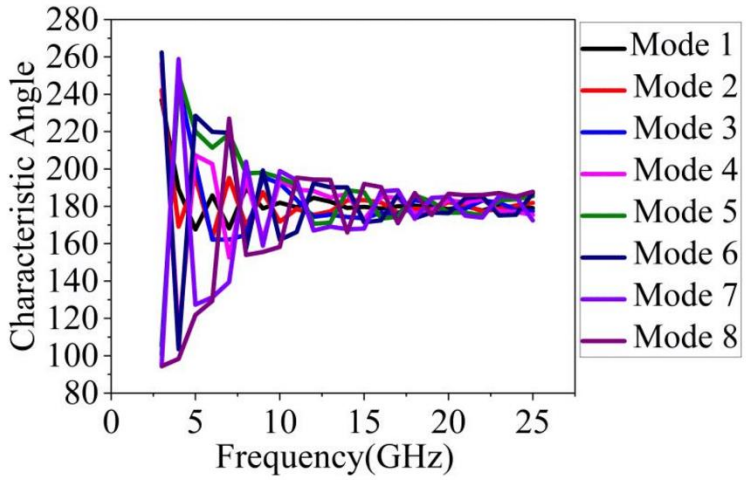

(a)

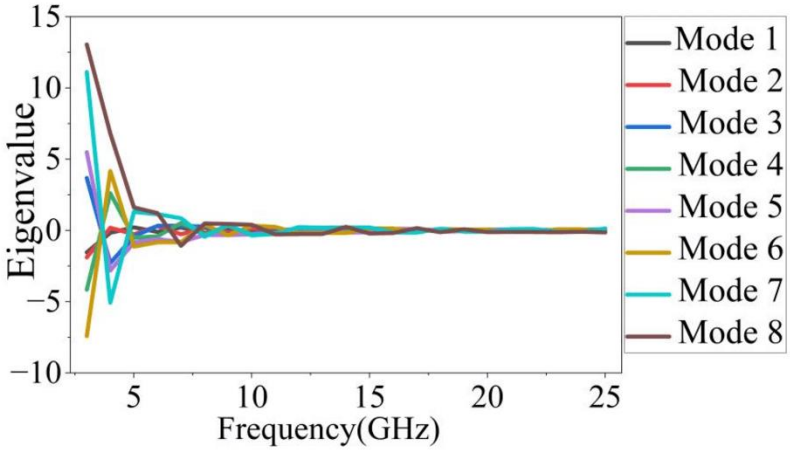

(b)

Fig. 6: Simulated results of (a) Characersitic angle, (b) Eigenvalue

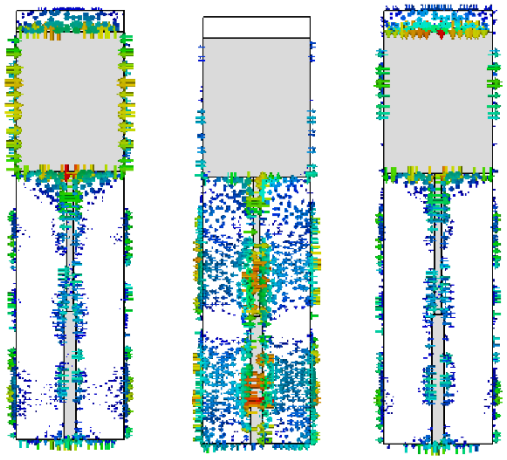

Fig 7: Field distribution of (a) Mode 1, (b) Mode 2, (c) Mode 3

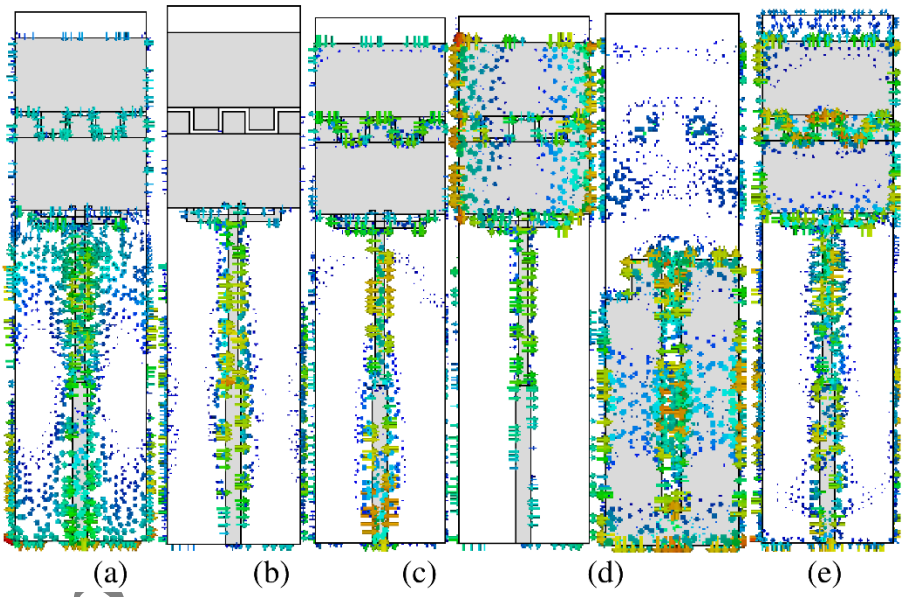

Fig. 8: Field distribution of (a) Mode 1, (b) Mode 2, (c) Mode 3, (d) Mode 4, (e) Mode 5

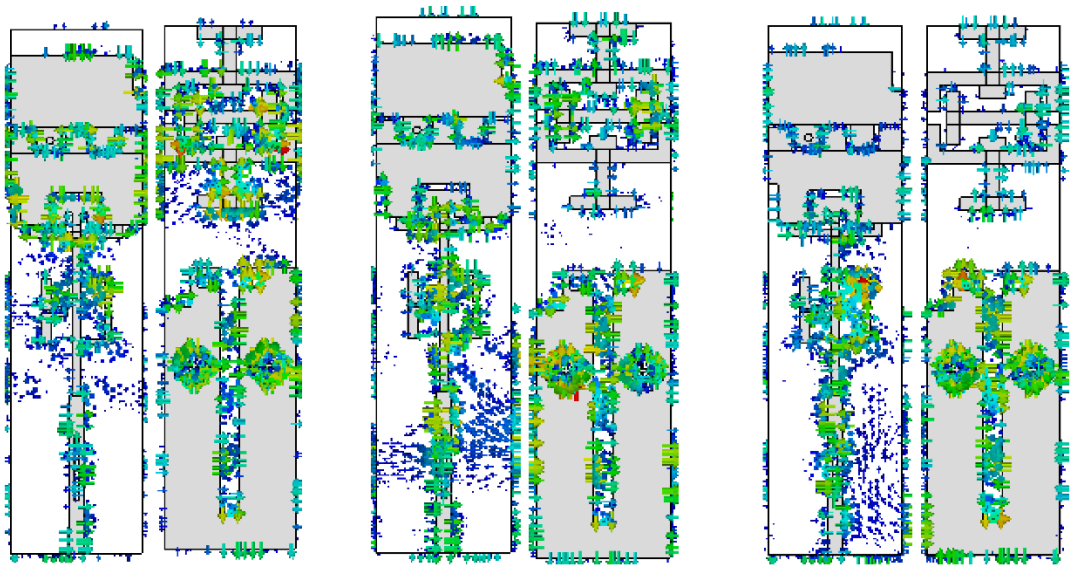

(a) (b) (c)

Fig. 9: Field distribution of (a) Mode 6, (b) Mode 7, (c) Mode 8

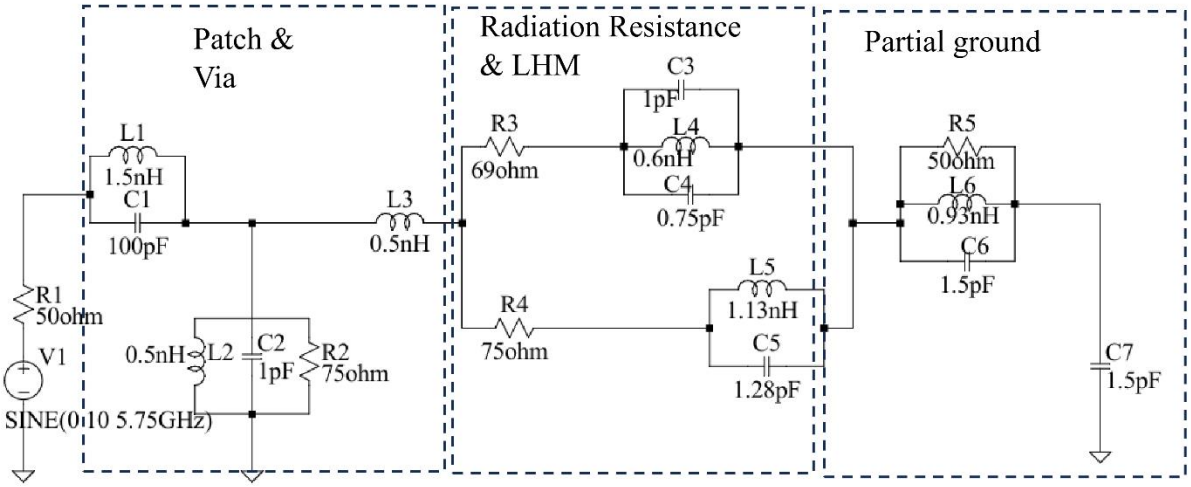

(a)

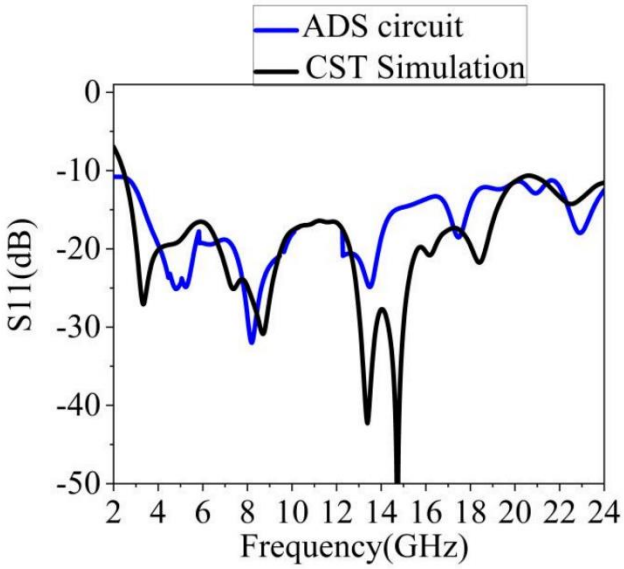

(b)

Fig. 10: Antenna (a) Equivalent circuit, (b) Circuit & schematic S11 comparison

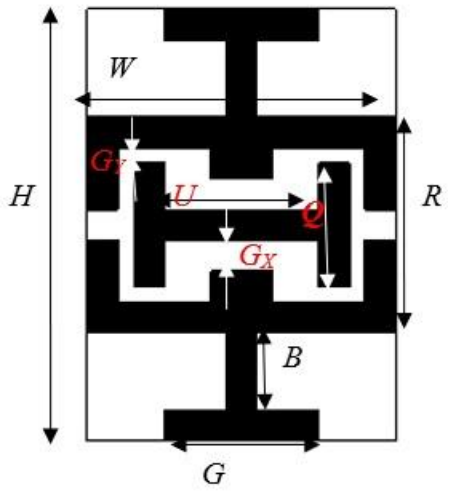

Fig. 11: LHM unit cell

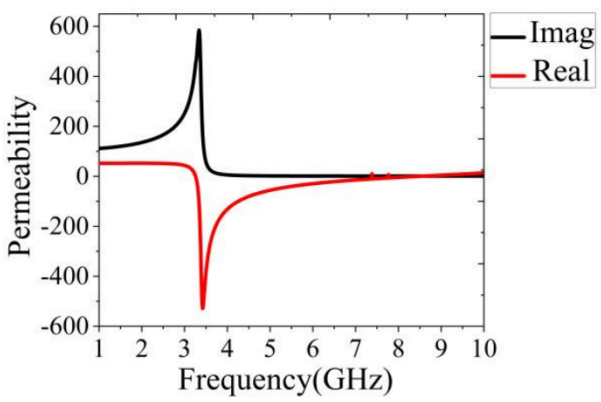

(a)

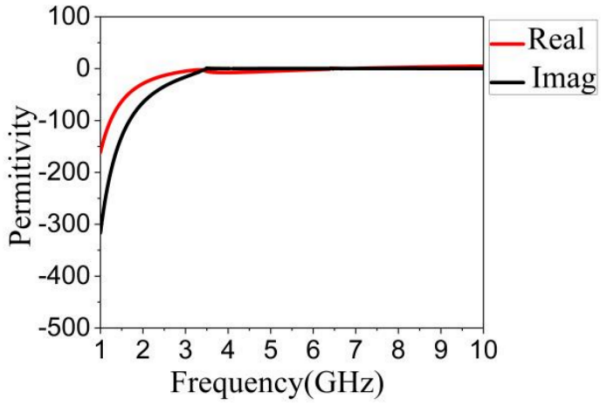

(b)

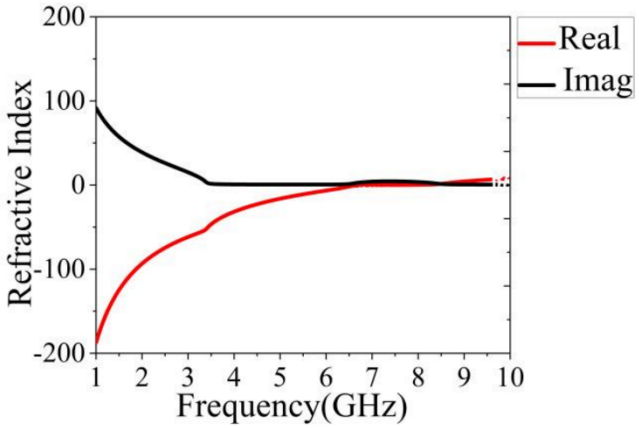

(c)

Fig. 12: Left hand metamaterial: (a) Permeability, (b) Permittivity, (c) Refractive index

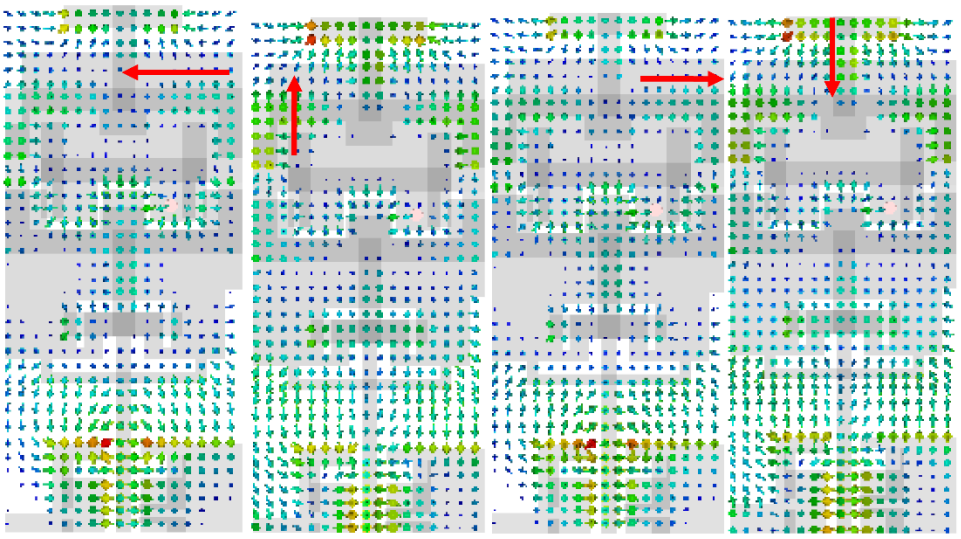

Fig. 13: Surface current direction for different phases of (a) 0°, (b) 90°, (c) 180°, (d) 270°

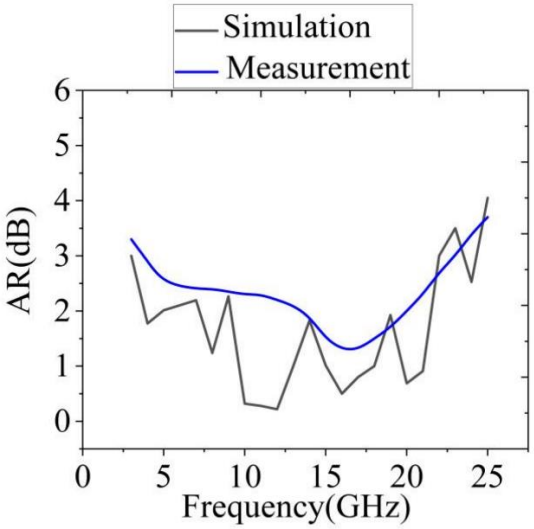

Fig. 14: AR graph

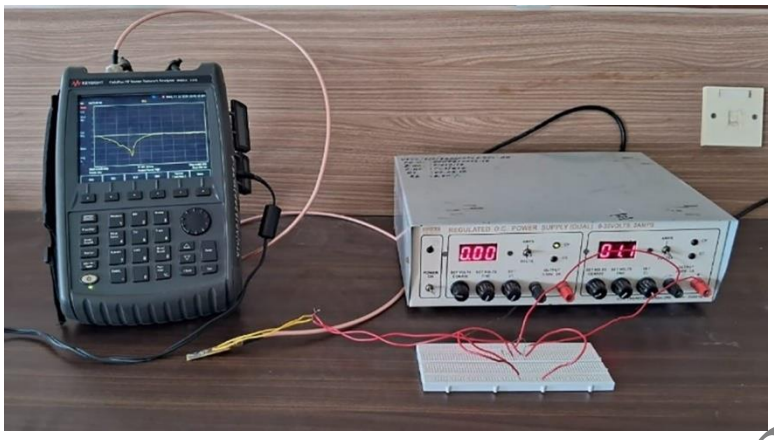

Fig. 15: Simulation and measurement of S11

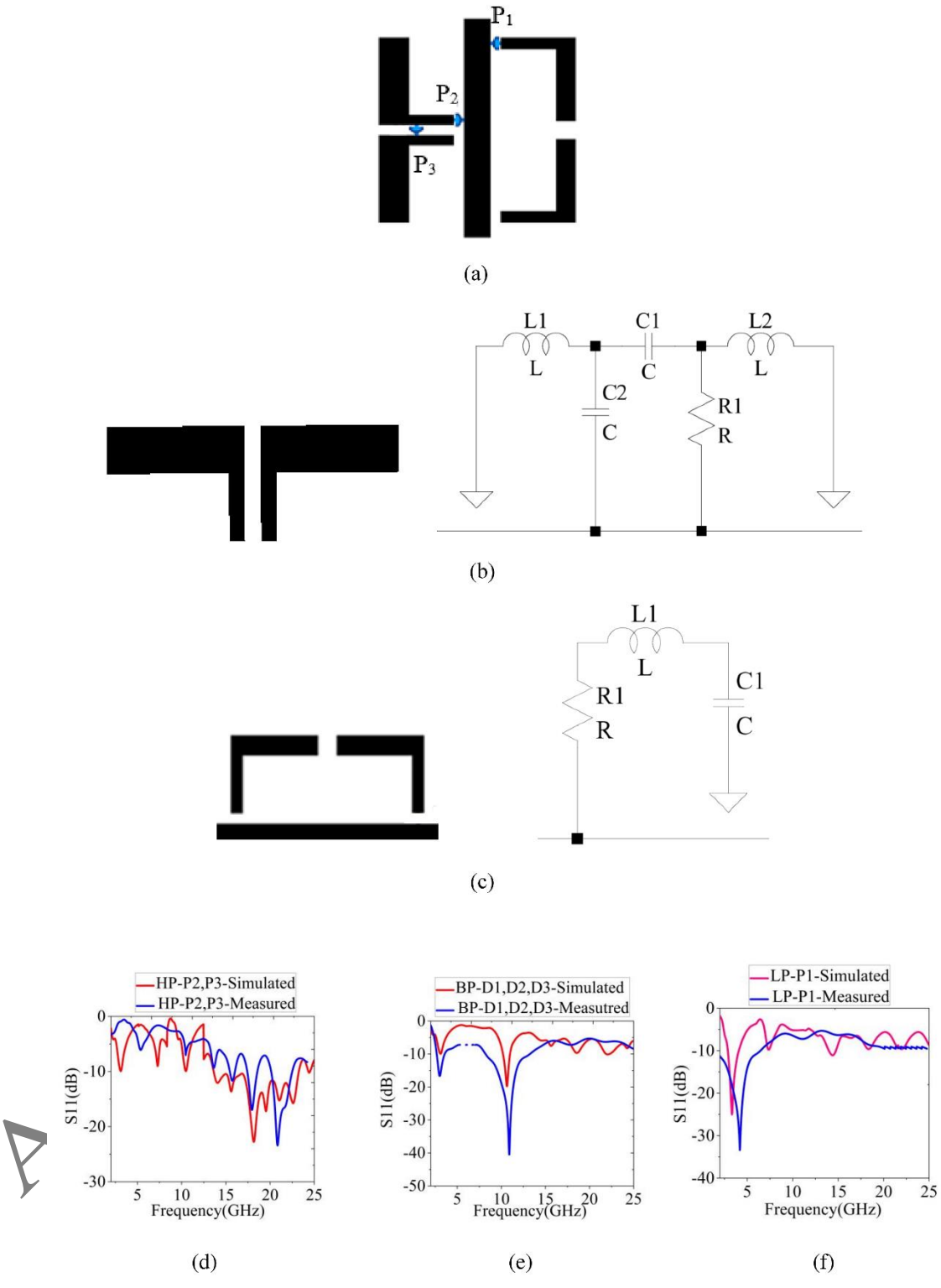

Fig.16: Reconfigurable filters (a) Reconfiguration filter (b) High pass filter, (c) Low pass filter (d) High-pass response, (e) Low-pass response, (f) Band-pass response

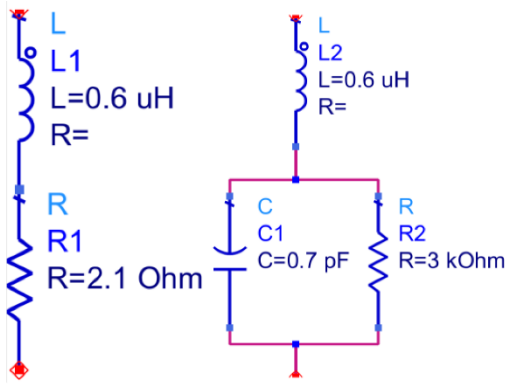

(a) (b)

Fig. 17: Equivalent circuit of pin diode in (a) ON state, (b) OFF state

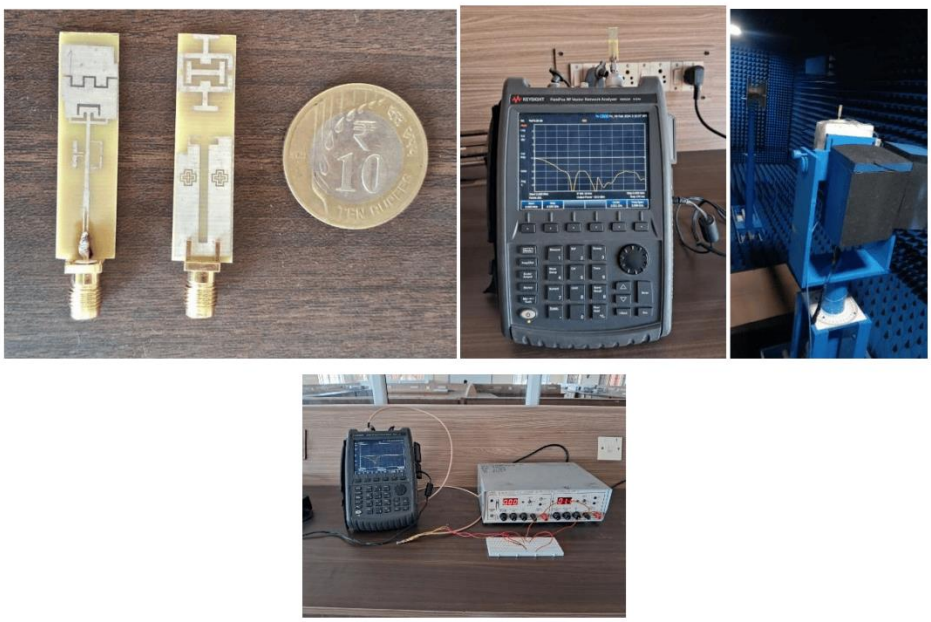

(a)

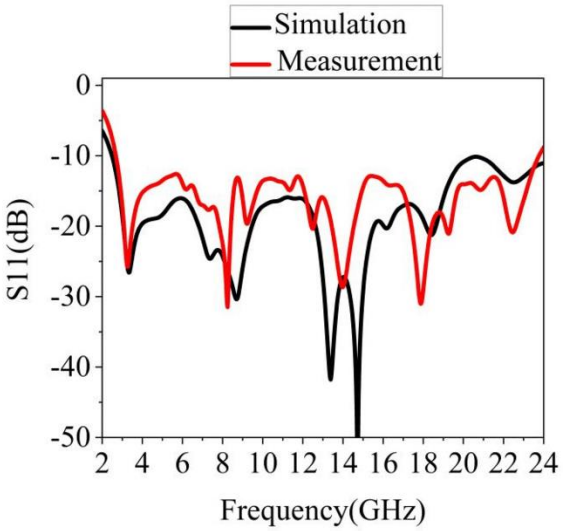

(b)

Fig. 18: The antenna (a) Fabricated layout with measuring arrangement, (b) S11 comparison

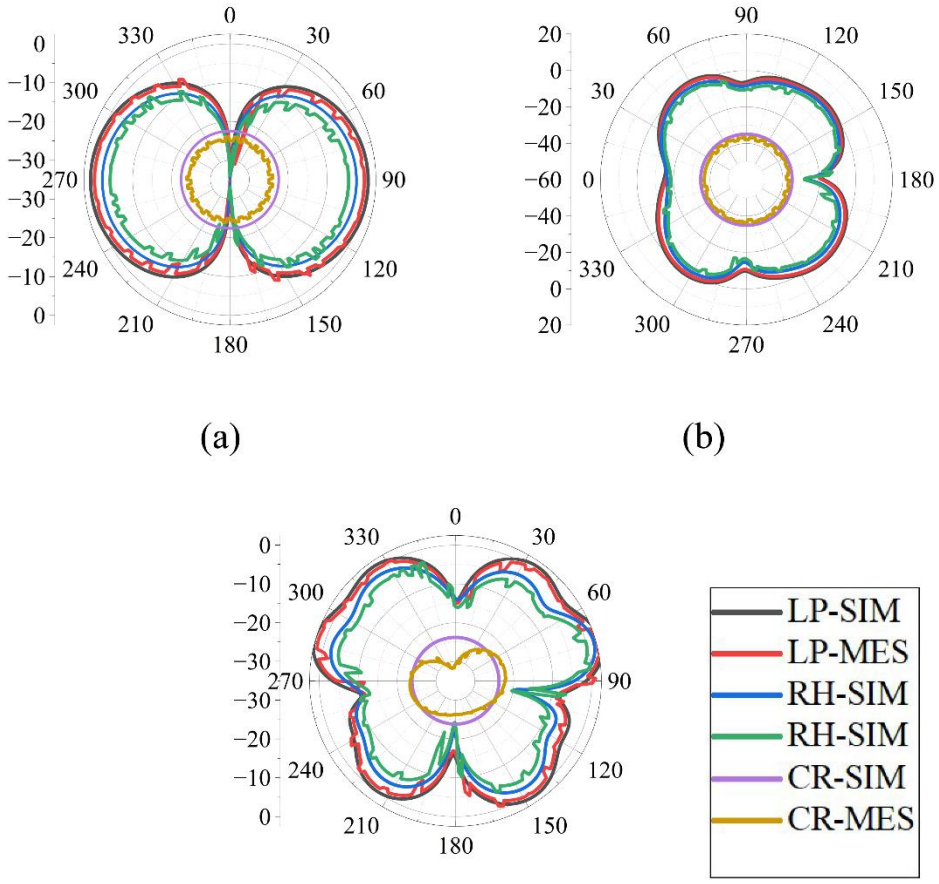

Fig. 19: E plane Radiation patterns at (a) 3GHz, (b) 11GHz, (c) 16GHz

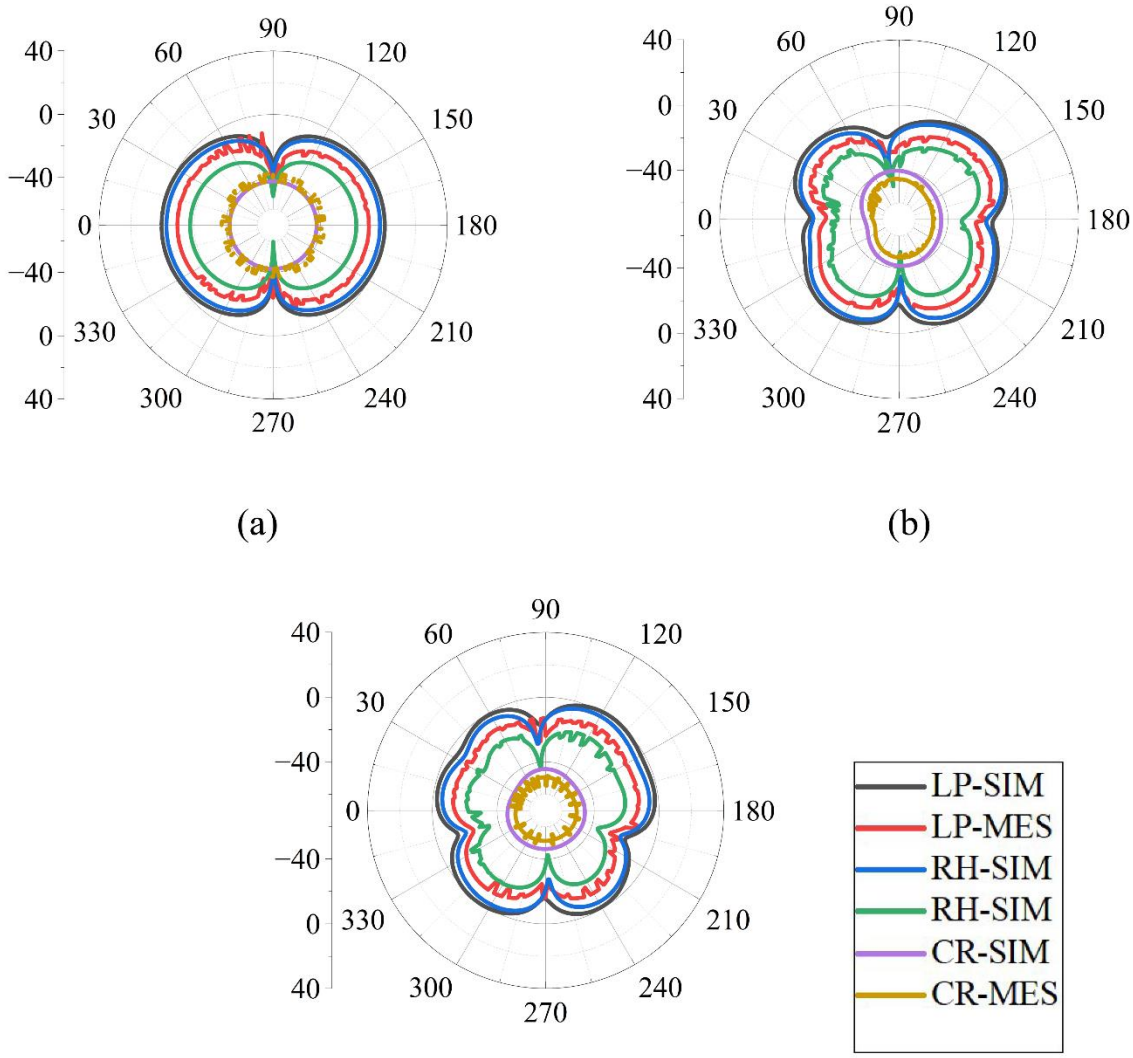

Fig. 20: H plane Radiation patterns at (a) 3GHz, (b) 11GHz, (c) 16GHz

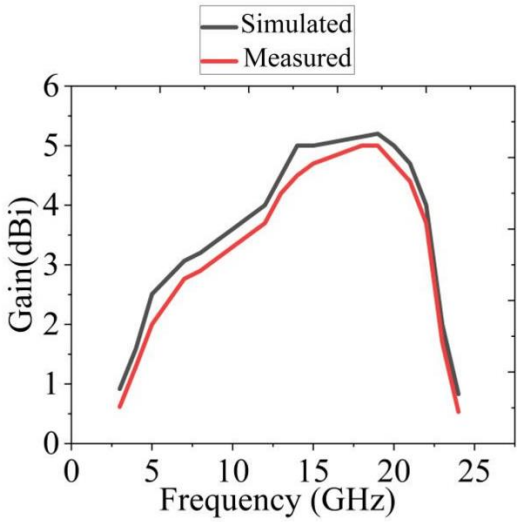

Fig. 21: Gain vs Frequency plot

Table 1: Modifications and their improvements

Modification	Improvement
LHM	LHM is placed directly behind the patch to enhance gain and promote circular polarization (CP)
Stub, steps, slit, and inset in the feed	To achieve improved impedance matching at lower frequencies up to 10GHz
Step slot in the patch	To achieve ultra-wideband coverage up to 16.2GHz, a step slot featuring consistent horizontal and vertical dimensions of C_1=2mm and C_2=2mm is utilized, which divides the resonant patch into two equal parts at its center.
Vertical slot in the ground	Improves the bandwidth that covers from 2.74 to 18.5GHz
EBG in ground	Extends the lower cutoff frequency f_l to 2.69GHz and renders better impedance matching at mid frequencies
Edge and longitudinal slots in ground	Enhances the bandwidth by 4GHz and supports circular polarization.
Reconfigurable Filter	To shift the bandwidth of operation
Corner asymmetric slots in patch	It brings asymmetric shape to the patch for supporting circular polarization

Table.2 Details of equivalent circuit

Physical Antenna Features	Equivalent Circuit Elements	Explanation
Patch		
Step slot	L_6, C_7	Long current path store magnetic energy, modeled as inductors. Electric fields across slots act like capacitive gaps, this produces parallel combination of inductance and capacitance.
Via	L_5, C_1, R_5	The finite conductivity of via contributes to both inductance and resistance, whereas the formation of parasitic capacitance with the patch and ground is represented by a capacitor.
Inverted U slot & Corner asymmetric slots	C_6	Inverted U slot induces capacitive effect which brings lower order modes close together and thus provides enhanced impedance matching at lower frequencies. The asymmetric slot perturbs the current distribution and couples different direction of current flow. The resultant electric field across the slot produces capacitance. The parallel combination this capacitance provides equivalent capacitance of C_6
Stub	L_1	Acting as a current path that establishes inductance
Dielectric	R_2	Substrate material which resists the current flow

		between top and bottom layer acts as a resistance
Left Hand Metamaterial (LHM)		
LHM	L_2, C_8, C_2	The LHM design renders electrical equivalent of parallel connection of inductance and capacitance
Radiation resistance	R_3	Models power actually radiated vs. dissipated.
Ground		
Vertical slot	L_4, C_4, R_6	C comes from the gap in the ground and L comes from the current path around the slot, R indicates diminishing current
EBG	L_3, C_3	This periodic slot behaves like a resonant LC network
Edge and longitudinal slots	C_5	The electric field across these slots induces couple of capacitances, whose parallel combination gives C_5

Table 3: Comparing of this research to the related article

	Polarization	**Max.Gain (dB)**	**Area**	**BW**	**Physical filters**	**Axial Ratio BW**
[1]	CP	3	$0.25\lambda_o^2$	7.5:1	Not used	2.85GHz
[2]	LP (Vertical)	4.2	$0.25\lambda_o^2$	3.24:1	Not used	NA
[4]	CP	3.27	$0.20\lambda_o^2$	1.21:1	Not used	0.74GHz
[3]	Nil	5.2	$0.04\lambda_o^2$	1.55:1	Used	Nil
[5]	CP	7	$0.325\lambda_o^2$	1.19:1	Used	0.22GHz
[6]	CP	5.2	$0.12\lambda_o^2$	1.03:1	Not used	0.5GHz
[9]	LP	8.7	$0.55\lambda_o^2$	1.27:1	Not used	Nil
[16]	CP	5.5	$0.15\lambda_o^2$	1.27:1	Not used	0.77GHz
[19]	Nil	7.2	$0.09\lambda_o^2$	3.6:1	Not used	Nil

Our Research	CP	5.28	$0.04\lambda_o^2$	8.54:1	Used	19GHz

Balu Ashvanth received his BE degree from Anna University Chennai in the year 2008, MTech degree from Pondicherry University in the year 2010 and PhD degree from Anna University Chennai in the year 2020. He is currently serving as an Associate Professor in the Department of Electronics and Communication Engineering, Vel Tech Rangarajan Dr.Sagunthala R&D Institute of Science and Technology, Chennai, India., His research areas of interest include analysis and design of antennas, absorbers and frequency selective surfaces for emerging applications

D. Kanchana is currently working as an Assistant Professor in the Department of Electronics and Communication Engineering at Sathyabama Institute of Science and Technology, Chennai, India. Her research interests include Frequency Selective Surfaces (FSS), Radio Frequency (RF) systems, and Antenna design. She has experience in designing conformal and wearable FSS structures and is actively involved in research related to advanced electromagnetic structures for communication and sensing applications.

Bactavatchalame Partibane received his BE degree in ECE from Madras University, Chennai, in 1999, and the MTech degree in ECE from Pondicherry University, Pondicherry, in 2003. Further, he obtained doctoral degree from Anna University, Chennai in 2017. He currently holds an

academic post as Associate Professor in the department of ECE, SSN Institutions. His research interests include Wireless Communication and Networks, Antenna Engineering and Security in Ad hoc and Sensor Network.